

Flexible All-biomass Gas Sensor based on Doped Carbon Quantum Dots/nonwoven Cotton with Discriminative Function

zhaofeng wu (✉ wuzf@xju.edu.cn)

Xinjiang University <https://orcid.org/0000-0002-1470-5648>

Min Zhang

Xinjiang University

Shuai Cao

Xinjiang University

Long Wang

Xinjiang University

Zhangjie Qin

Xinjiang University

Furu Zhong

Zunyi Normal College

Haiming Duan

Xinjiang University

Research Article

Keywords: Cotton fiber, Carbon quantum dot, Expired milk, Flexible gas sensor, Discriminative detection

Posted Date: August 24th, 2021

DOI: <https://doi.org/10.21203/rs.3.rs-753011/v1>

License:   This work is licensed under a Creative Commons Attribution 4.0 International License.

[Read Full License](#)

Abstract

Carbon quantum dots (CQDs) co-doped with N, P and S derived from expired milk was prepared by a simple hydrothermal method. Through the hydrogen bond interaction between CQDs and cellulose of pure cotton face towel (PCFT), CQDs were uniformly anchored on the cotton fibers to form a flexible all-biomass CQDs/PCFT sensor for the first time. Due to the heteroatom doping, extremely small particle size of CQDs and excellent permeability of CQDs/PCFT film, the flexible CQDs/PCFT sensor showed the high sensitivity and bending stability. In the range of 0 ~ 60° bending states, the responses of flexible CQDs/PCFT sensor to four target analytes changed by less 5%. Interestingly, due to the abundant functional groups and defects of CQDs, the flexible CQDs/PCFT sensor displayed sensing curves of different shapes for different target analytes. In this way, by establishing a database of sensing curves of target analytes, multiple analytes can be detected discriminatively by relying only on single sensor with the help of image recognition. In addition, the binary parameter method of response and response time was created, which also showed that a single sensor could achieve the discriminative detection. This work expanded the application of biomass CQDs and cellulose, and made a useful exploration for environment friendly flexible gas sensor.

Introduction

In recent years, with the gradual increase of people's attention to health, safety and environmental protection, flexible gas sensors have received more attention (Liu et al. 2014; Gao et al. 2016; Falco et al. 2018). Generally, the gas sensor with the higher sensitivity and faster response/recovery speed was expected (Franke et al. 2006). According to the classical theory, the smaller the particle size of sensing materials, the higher the sensitivity (Schierbaum et al. 1991; Göpel 1995; Franke et al. 2006). In principle, a reduction in the particle size of the sensing material at the nanoscale would significantly increase the number of structural and electronic defects of the sensing materials (Franke et al. 2006; Liu et al. 2014). In the sensing process, these defects act as adsorption sites and reactive sites to enhance the sensing performance of the sensing materials (Liu et al. 2014; Wu et al. 2016). Therefore, the high sensitivity has been expected for the sensing materials with small particle size.

Quantum dots (QDs) are an important low-dimensional semiconductor material with diameters ranging from 2 to 20 nm (Alivisatos 1996; Klimov et al. 2000). It can be seen that QD materials are very suitable for gas sensors due to the very small particle size and very high specific surface area. Common QDs, such as CdS, CdSe, CdTe, ZnSe, PbS and PbSe, are often used in the fields of fluorescence sensing (Wang et al. 2012; Kini et al. 2018; Ren et al. 2018), imaging (Hao et al. 1999; Silva et al. 2016) and solar cells (Fuke et al. 2010; Baines et al. 2018) because of their unique optical properties. However, these QD materials often contain toxic elements (Cd, Pb), thus their large-scale applications would raise some potential environmental concerns. In addition, some QDs (XSe, XTe QDs, X = Cd, Zn, Pb) are less chemically stable and easily oxidized, which are not suitable for prolonged exposure to the air. Therefore, considering the environmental protection and chemical stability, the traditional QD materials are not suitable for gas sensors. Recently, biomass carbon quantum dots (CQDs) have attracted more and more

attentions due to the advantages of abundant raw materials, simple preparation, low cost and non-toxic. Because of the excellent optical properties and high chemical stability, biomass CQDs are used in bioimaging (Wang et al. 2016; Hu et al. 2017; Meena et al. 2019), biosensing (Wang et al. 2016; Abbas et al. 2018; Ding et al. 2018; Qi et al. 2019), solar cells (Briscoe et al. 2015; Liu et al. 2019) and photocatalysis (Fernando et al. 2015; Das et al. 2019). However, the application of biomass CQDs in the field of chemiresistive gas sensor has not been reported. In addition, it is well known that atomic doping is a common and effective method to improve the gas sensitive properties of sensing materials (Franke et al. 2006; Wu et al. 2016). Because biomass material itself contains a variety of elements, it is convenient to prepare heteroatomic doped CQDs. Heteroatom doping of CQDs provides more active sites to broaden their potential applications in the analysis and sensing (Hu et al. 2017; Qi et al. 2019).

However, CQDs are easy to agglomerate due to their small particle size and high surface energy, which is not conducive to play its advantage of large surface area to improve the gas sensing performance (Deng et al. 2013). Currently, plastic and rubber were often used as the flexible sensing substrates of gas sensors to support sensing materials (Bai et al. 2015; Wang et al. 2017; Zhang et al. 2020). Unfortunately, plastic and rubber displayed poor gas permeability, which prevented the effective contact between the sensing material and the target gas, and limited the gas sensing performance (Liu et al. 2014; Zhang et al. 2020). What's more, plastic and rubber can hardly degrade, or take hundreds of years to degrade (Robinson 2009; Wang et al. 2017). In sharp contrast, the average service life of electronic devices, such as gas sensors and flexible displays, is only about 18 months (Robinson 2009; Wang et al. 2017). As a result, a large amount of solid waste is produced by the failure of gas sensors, which brings potential harm to the environment. As far as sensing substrates are concerned, biomass materials also show the incomparable advantages over rubber and plastics. For example, cotton fabric, cotton-based nonwovens and filter paper are increasingly used as flexible sensing substrates because of its renewable, degradable properties, low price, good flexibility and high gas permeability (Liu et al. 2014; Zhang et al. 2020). These biomass-fiber structures not only endow the gas sensor with good flexibility, but also improve the gas permeability of the sensing substrate, enhancing the gas sensing performance (Liu et al. 2014; Zhang et al. 2020). What's more, these renewable and degradable biomass fibers do not need to consume any petrochemical raw materials, which is beneficial to environmental protection and sustainable development.

In this work, in order to realize the resource utilization of waste, CQDs co-doped with N, P and S derived from expired milk was prepared by a simple hydrothermal method. Pure cotton face towel (PCFT), as a sensing substrate, was soaked in the biomass CQDs ink and dried to make a CQDs/PCFT film by means of hydrogen bond interaction between CQDs and cellulose of PCFT. The CQDs/PCFT film was used as an all-biomass flexible gas sensor for the first time, showing high sensitivity and bending stability. More importantly, due to the abundant functional groups and atomic doping of CQDs, the flexible gas sensor has displayed sensing curves of different shapes for different target analytes, which lays a foundation for the discriminative detection of multiple analytes by relying only on single sensor and image recognition.

Experimental

Materials

Ethanol (C₂H₆O), formaldehyde (CH₂O), acetone (C₃H₆O), ammonia (NH₃) was purchased from Sinopharm Chemical Reagent Co., Ltd., Beijing, China. Pure cotton face towel (PCFT) is purchased from Karedelle (Shenzhen, China) Technology Development Co. Ltd. The milk was purchased from Henan Shanjianke (Luohe, China) Agriculture Co., Ltd.

Preparation of CQD ink and flexible CQD/PCFT sensor

First, 35 mL of expired milk was measured and put into a 50 mL PTFE reactor, then sealed and placed in a 180 °C oven for 8 h. Secondly, when the temperature of the reactor dropped to room temperature, the liquid in the reactor was centrifuged at 8000 RPM for 10 min, and the yellow supernatant was retained, which was known as the CQD ink. Thirdly, the PCFT film was cut into 5×30 mm² strips. The strips were immersed in CQD ink for 3 min and then taken out to dry at room temperature, forming the CQD/PCFT film. At last, the CQD/PCFT film was then cut into 2×13 mm² strips to test its gas-sensitive performance as a flexible gas sensor.

Gas sensitive test of flexible CQD/PCFT sensor

The testing process of gas sensors for various target atmospheres was similar to the previous reports (Zhang, Wu et al. 2020). The gas sensing performances of flexible CQD/PCFT sensor were tested by the CGS-MT Multi-functional Probe Station at room temperature (25 ± 1 °C). During the gas sensitive test, a voltage of 4 V was applied to both ends of flexible CQD/PCFT film and the relative humidity (RH) of the test room was controlled to be 35 ± 2% through the air conditioning system. The response of electric current is defined as, $\text{Response} = I_G/I_A$, where I_A and I_G are the electric current of the sensor in air and in target gas, respectively. The response time and the recovery time is defined as same as earlier reports (Zhang et al. 2020).

Characterization

The morphology of samples was characterized by field emission scanning electron microscopy (FE-SEM, S-4800, Hitachi, Japan) equipped with an energy-dispersive X-ray spectrometer (EDX), transmission electron microscope (JEOL JEM-2100 F) and optical microscope (BX53M, Olympus). The structure of samples was characterized by X-ray diffraction (XRD, Bruker D8 Advance, with Cu-K α radiation), Raman spectra (SENTERRA Compact Raman Microscope), and Fourier Transform Infrared (FT-IR, Bruker VERTEX70, Germany). Fluorescence spectra and UV-Vis absorbance spectra were acquired a Hitachi F4600 spectrometer (Hitachi, Tokyo Japan) and UV-3900H spectrometer (Hitachi, Japan).

Results And Discussion

The UV-Vis absorption spectrum in Fig. 1a shows the CQDs has an absorption peak at 284 nm, resulting from the π - π^* transition of C = C (Pan et al. 2010). As shown by the inset in Fig. 1a, the CQDs ink is brown-yellow and the CQDs ink glows green irradiated with 365 nm of light. As shown in Fig. 1b, the excitation spectrum of CQDs ink was measured at an emission wavelength of 400 nm, which showed that the CQDs ink had the highest absorption at about 450 nm. The fluorescence (FL) emission spectra of the CQDs ink excited at 390, 410, 420, 430, 440, 450 and 460 nm. These FL emission spectra showed an increase in intensity and a red shift in the wavelength of peak emission. When the wavelength of the excited light reached 450 nm, the emission intensity of CQDs ink reached the maximum. These excitation-dependent behaviors could be attributed to the optical selection of different-sized nanoparticles or different surface emissive traps (Liang et al. 2016). The TEM image shows that CQDs has good dispersion and uniformity (Fig. 1c). The HRTEM image shows the relatively clear lattice fringes (Fig. 1d) and the lattice spacing of 0.3 nm (the insert in Fig. 1d), which is consistent with the (002) diffraction facets of graphite diffraction (Dong et al. 2013). By randomly calculating 50 particles, the particle size distribution is obtained. The calculation results show that the particle size distribution of CQDs was in the range of 2 ~ 6 nm, of which 3.5 nm CQDs accounted for the highest proportion (Fig. 1e). The FT-IR spectrum shows the CQDs has rich functional groups (Fig. 1f). The peak appearing at around 3316 cm^{-1} corresponds to the OH/NH bond, and the peaks at 1668 and 1745 cm^{-1} are attributed to the stretching vibration of C = O in aromatic aldehydes (Hu et al. 2017). The peak at 1158 cm^{-1} corresponds to the C = N, C = S and C = O bonds (Hu et al. 2017) and the peaks at 2925 and 2854 cm^{-1} correspond to stretching vibration of CH/CH₂. The peak at 1460 cm^{-1} corresponds to the bending vibration peak of CH/NH. The peak at 776 and 702 cm^{-1} correspond to the CH bending vibration of the benzene ring. The abundant functional groups of CQDs can improve the interaction between CQDs and various target gases. The main component of cotton fiber is cellulose, containing a large number of hydroxyl groups (Zhang et al. 2020). At the same time, the N, O and S contained in the CQDs form hydrogen bond with the H atom in hydroxyl groups of cellulose, which is convenient for the CQDs to adsorb on cotton fiber, forming the stable CQD/PCFT film.

As shown in Fig. 2a-d, the cotton fibers of PCFT film were in the state of nonspinning, namely the state of disorderly, which increased its specific surface area and gas permeability. After further magnification (Fig. 2c-d), the diameter of the cotton fibers was about a dozen microns. The optical images of PCFT film were white, while the CQD/PCFT film was yellow, indicating that the CQDs uniformly adhered to the cotton fibers. As shown by SEM images in Fig. 2e, f, it can be clearly seen that the surfaces of cotton fibers in PCFT and CQD/PCFT film were wrinkled. However, no CQDs were found on the cotton fibers of CQD/PCFT film, possibly because the particle size of the CQDs was too small to be easily observed.

As shown in Fig. 3a-f, the element distribution showed that pure cotton fiber of PCFT contained only C and O, but no N, P and S. The results of element analysis were consistent with the fact that cotton fiber was mainly composed of cellulose (Jonoobi et al. 2015; Zhang et al. 2020). It is well known that milk contains proteins, which contain N, P and S, so the CQD derived from milk also contain N, P and S. As shown in Fig. 3g-l, there are not only C and O elements, but also N, P and S elements on the surface of cotton fiber soaked by CQDs ink, and these elements are evenly distributed on the CQD/PCFT fibers,

indicating that CQDs are uniformly adsorbed on the surface of cotton fibers through hydrogen bond between CQDs and cellulose (Fig. 3m). This is consistent with the results of optical microscopy (Fig. 2c, d) and FT-IR spectra of CQDs (Fig. 1f). The small size of CQDs, the excellent flexibility of cotton fibers and the uniform adsorption of CQDs lay the foundation for the flexible gas sensor. At the same time, the doping of a variety of heterogeneous atoms will have a significant effect on the gas sensitive properties.

According to the XRD data in Fig. 4a, the pure PCFT exhibited a strong peak at 23.1° and two weak peaks at 15.1° and 16.5° , respectively. This is consistent with the reported structure of pure cotton (Zhang et al. 2020). Compared with the PCFT film, the structure of the CQD/PCFT film did not change significantly. This might be because the crystallinity of the micron-scale cotton fiber was good, while the crystallinity of the nanoscale CQDs was poor, and only a very thin layer of CQDs was on the cotton fiber, so the characteristic peak of the CQDs was not seen. However, compared with the PCFT film, the Raman spectra and UV-Vis spectra of the CQD/PCFT film changed obviously (Fig. 4b, c). Compared with the PCFT film, there were two weak characteristic peaks (G band at 1580 cm^{-1} and D band at 1375 cm^{-1} in Fig. 4b) of carbon materials on Raman spectra of CQD/PCFT film (Cao et al. 2021). As shown in Fig. 4c, the light absorption of CQD/PCFT film in the UV region was significantly enhanced, which indicated that the CQD/PCFT film had the potential of making UV shielding clothing. As can be seen from the inserts of Fig. 4c, the PCFT film was white, while the CQD/PCFT film was pale yellow, which was consistent with the light microscope observation (Fig. 2a-d). These results proved that a thin layer of CQDs was uniformly coated on the cotton fibers, forming the CQD/PCFT composite film.

To evaluate the gas-sensitive performance of the flexible CQD/PCFT sensor, six target gases were tested. As shown in Fig. 5, without bending, the flexible CQD/PCFT sensor showed the excellent sensing capability for the 85% RH, NH_3 , H_2O_2 and CH_2O vapor, and extremely low sensitivity for $\text{C}_2\text{H}_6\text{O}$ and $\text{C}_3\text{H}_6\text{O}$ vapor. Interestingly, the shapes of the sensing curves of the CQD/PCFT sensors to the 85% RH, NH_3 , H_2O_2 and CH_2O were different, which might be able to realize the discriminative detection. This may be related to the fact that the rich functional groups in CQDs, like the various components in an army knife, allow CQDs to react specifically with a variety of target gases and produce sensing curves of different shapes. Previous discriminative detection often relied on a sensor array or electronic nose containing multiple sensors, and then through data processing such as principal component analysis and radar map analysis could be realized (Sun et al. 2019). Nowadays, with the development of big data and image recognition technology, the discriminative detection of target vapor can be realized through single sensor producing different sensing images corresponding to different target vapors.

As shown in Fig. 6, the bending stability of the flexible CQD/PCFT sensor was also tested. The bending angle indicated in the bending test was shown by the insert in Fig. 6a. When the bending angle was 90° , it corresponded to the folded state of the flexible sensor. As shown by Fig. 6a, the current of the flexible sensor was about 18 nA, and there was no significant fluctuation with the increase of bending angles. It can be clearly seen from Fig. 6b-e, at bending angles of 0° , 30° and 60° , the sensing curves of 85% RH, NH_3 , H_2O_2 and CH_2O did not change significantly, showing good bending stability. As can be seen from

the statistical data in Fig. 6f, g, under the three bending states, the responses of the four target analytes changed by less than 5%, and the response time changed by less than 20%, also showing good bending stability. At the same time, the flexible CQD/PCFT sensor also demonstrated rapid recovery ability, and the recovery times were less than 2 s for all four analytes.

Discriminative detection has always been a bottleneck for gas sensor and sensor arrays and electronic noses have been used to break through this bottleneck (Gao et al. 2016; Wu et al. 2016). However, sensor arrays required higher cost and power consumption, because of the built-in multiple sensors. Therefore, the average response and response time of each analyte under three bending angles (Fig. 6h) are used as a binary parameter (Response time, Response) to evaluate the identification capability of the flexible CQD/PCFT sensor. As shown in Fig. 6h, except for the 85% RH and CH₂O, the binary parameters of other analytes are very different. This means that with the help of binary parameters (Response time, Response), a single sensor also shows some identification capability, but it still needs to be improved. It is worth noting that the flexible CQD/PCFT sensor maintains a high resolution of the shapes of the sensing curves for the four analytes despite the bending states. Additionally, the technologies of image recognition and cloud storage have developed rapidly in recent years. Therefore, we assume that the sensing curves from the flexible CQD/PCFT sensor are stored as a graph in the cloud database to form a database of sensing graphs (Fig. 6i). Then, with the aid of image recognition technology, the sensing graph of the unknown vapor is compared with the cloud database, and finally the unknown gas could be identified (Fig. 6i). In this way, it is possible to identify and detect a variety of analytes with single sensor and image recognition technology.

The classical theory holds that the sensitivity of the chemiresistive gas sensor is related to the particle size (D) of the sensing material and the charge depletion layer depth (L) (Schierbaum et al. 1991; Göpel 1995; Franke et al. 2006). As shown by Fig. 7a, c, the charge depletion layer was formed because oxygen molecules attached to the sensing particle took electrons from the sensing particle, forming oxygen anions (O^{2-} , O^- or O_2^-) (Schierbaum et al. 1991; Göpel 1995; Franke et al. 2006). Figure 7a, c show that small sensing particles formed a deeper charge depletion layer (L) in the air than large sensing particles, which also generated a higher surface potential barrier (eV_{surface}) in the small sensing particles. Take CH₂O vapor for example, during the sensing process, when the CH₂O molecules were attached to the surfaces of CQDs, the following reaction occurred at room temperature:



When the CH₂O molecule adsorbed on the sensing particle, it released electrons to the N-type sensing material, which made the charge depletion layer thin (Fig. 7b, d). However, for small sensing particles, the change of charge depletion layer was more significant than that for large sensing particles (Schierbaum et al. 1991; Göpel 1995; Franke et al. 2006). Accordingly, the change of the surface barrier ($\Delta eV_{\text{surface}}$) of the small sensing particle was much more obvious than that of the large sensing particle. It has been

reported that the conductance G of the sensing material is exponentially proportional to the effective barrier height (Franke et al. 2006; Li et al. 2015; Zhang et al. 2018).

$$G \approx \exp(-eV_{\text{surface}}/kT) \quad (2)$$

Where eV_{surface} is the effective potential barrier, k is Boltzmann's constant and T is absolute temperature. It can be seen that a small change in the effective barrier will cause a significant change in the conductance G of sensor. The conductance of the sensing material in the air and the target vapor corresponds to I_A and I_G , respectively. According to the definition of Response (Response = I_G/I_A), small sensing particles will be more sensitive to target vapor than large sensing particles (Schierbaum et al. 1991; Göpel 1995; Franke et al. 2006).

In the case of CQDs/PCFT film, the excellent gas sensing performance should be attributed to the synergistic effect between CQDs and f PCFT film (Fig. 7e). First, the particle size of CQDs was very small, basically less than 10 nm. Second, the CQDs had a highly defective graphene structure, especially those with heteroatomic doping (Wang et al. 2016; Hu et al. 2017; Qi et al. 2019). Due to the doping of N, P, S, and the rich functional groups, CQDs had more adsorption and reaction sites (Hu et al. 2017; Qi et al. 2019), which was beneficial to increase the charge depletion layer depth L (Fig. 7e). Third, the particle size of nanoparticles was small, their surface energy was high, and nanoparticles tended to stick together to reduce surface energy (Alivisatos 1996; Klimov et al. 2000). As a result, the advantage of large specific surface area of nanoparticles was not exploited. The CQDs were attached to the cotton fibers of the CQDs/PCFT film, which avoided agglomeration of CQDs and allowed the CQDs to take advantage of the large specific surface area and the rich functional groups. Fourth, the CQDs/PCFT film with the high permeability facilitated the adsorption and desorption of gas molecules, which was also very important to improve the performance of the gas sensor (Liu et al. 2014; Zhang et al. 2020). The above aspects contributed together to the excellent gas sensing performance of CQDs/PCFT film.

Conclusions

CQDs co-doped with N, P and S derived from expired milk was prepared by a simple one-step hydrothermal method. PCFT as the sensing substrate was soaked in the CQDs ink and dried to make a flexible all-biomass CQDs/PCFT sensor by means of hydrogen bond interaction between CQDs and cellulose of PCFT for the first time. Due to the doping of N, P and S, high specific surface area, extremely small particle size, uniform dispersion of CQDs and excellent permeability of the CQDs/PCFT, the flexible CQDs/PCFT sensor showed the high sensitivity and bending stability in the range of 0 ~ 60°. Importantly, the flexible sensor has displayed sensing curves of different shapes for different target analytes, which lays a foundation for the discriminative detection of multiple analytes by relying only on single sensor and image recognition. In addition, the binary parameter method of response and response was created, which also showed that a single sensor could show good capability of discriminative detection. This

work expanded the application of biomass CQDs and cellulose, and made a useful exploration for environment friendly flexible gas sensor.

Declarations

Acknowledgements

This research was funded by Natural Science Foundation of Xinjiang Uygur Autonomous Region (2019D01C019, XJEDU2020Y004), National Natural Science Foundation of China (21964016, 11664038, 61864011), and Tianshan Innovation Team Program of Xinjiang Uygur Autonomous Region (2020D14038).

Author contributions

Zhaofeng Wu and Min Zhang conceived and designed the experiment; Shuai Cao, Long Wang and Zhangjie Qin carried out the experiment, processed the data and wrote the first draft; Zhaofeng Wu, Min Zhang, Furu Zhong and Haiming Duan contributed to scientific discussion and modification of the manuscript.

Availability of data and materials

None

Conflict of interest

The author declares that they have no conflict of interest.

Ethical standards

This study following Compliance with Ethical Standards; this study does not involve human participants, animals, and potential conflicts of interest.

References

1. Abbas A, Mariana LT, Phan AN (2018) Biomass-waste derived graphene quantum dots and their applications. *Carbon* 140:77–99. <https://doi.org/10.1016/j.carbon.2018.08.016>
2. Alivisatos AP (1996) Semiconductor clusters, nanocrystals, and quantum dots. *Science* 271:933–937. <https://doi.org/10.1126/science.271.5251.933>

3. Bai S, Sun C, Wan P, Wang C, Luo R, Li Y, Liu J, Sun X (2015) Transparent conducting films of hierarchically nanostructured polyaniline networks on flexible substrates for high-performance gas sensors. *Small* 11:306–310. <https://doi.org/10.1002/sml.201401865>
4. Baines T, Zoppi G, Bowen L, Shalvey TP, Mariotti S, Durose K, Major JD (2018) Incorporation of CdSe layers into CdTe thin film solar cells. *Sol Energy Mater Sol Cells* 180:196–204. <https://doi.org/10.1016/j.solmat.2018.03.010>
5. Briscoe J, Marinovic A, Sevilla M, Dunn S, Titirici M (2015) Biomass-derived carbon quantum dot sensitizers for solid-state nanostructured solar cells. *Angew Chem Int Ed* 54:4463–4468. <https://doi.org/10.1002/anie.201409290>
6. Cao S, Wu Z, Sun Q, Zhang W, Beysen S, Wang S, Shaymurat T, Zhang M, Duan H (2021) Gas sensing properties of cotton-based carbon fibers and ZnO/carbon fibers regulated by changing carbonization temperatures. *Sens Actuators B* 337:129818. <https://doi.org/10.1016/j.snb.2021.129818>
7. Das GS, Shim JP, Bhatnagar A, Tripathi KM, Kim T (2019) Biomass-derived carbon quantum dots for visible-light-induced photocatalysis and label-free detection of Fe(III) and ascorbic acid. *Sci Rep* 9:15084. <https://doi.org/10.1038/s41598-019-49266-y>
8. Deng XL, Davé RN (2013) Dynamic simulation of particle packing influenced by size, aspect ratio and surface energy. *Granular Matter* 15:401–415. <https://doi.org/10.1007/s10035-013-0413-0>
9. Ding Z, Li F, Wen J, Wang X, Sun R (2018) Gram-scale synthesis of single-crystalline graphene quantum dots derived from lignin biomass. *Green Chem* 20:1383–1390. <https://doi.org/10.1039/C7GC03218H>
10. Dong Y, Pang H, Yang HB, Guo C, Shao J, Chi Y, Li CM, Yu T (2013) Carbon-based dots Co-doped with nitrogen and sulfur for high quantum yield and excitation-independent emission. *Angew Chem Int Ed* 52:7800–7804. <https://doi.org/10.1002/anie.201301114>
11. Falco A, Rivadeneyra A, Loghin FC, Salmeron JF, Lugli P, Abdelhalim A (2018) Towards low-power electronics: self-recovering and flexible gas sensors. *J Mater Chem A* 6:7107–7113. <https://doi.org/10.1039/C7TA11311K>
12. Fernando KAS, Sahu S, Liu Y, Lewis WK, Gulians EA, Jafariyan A, Wang P, Bunker CE, Sun YP (2015) Carbon quantum dots and applications in photocatalytic energy conversion. *ACS Appl Mater Interfaces* 7:8363–8376. <https://doi.org/10.1021/acsami.5b00448>
13. Franke ME, Koplín TJ, Simon U (2006) Metal and metal oxide nanoparticles in chemiresistors: Does the nanoscale matter? *Small* 2:36–50. <https://doi.org/10.1002/sml.200500261>
14. Fuke N, Hoch LB, Kuposov AY, Manner VW, Werder DJ, Fukui A, Koide N, Katayama H, Sykora M (2010) CdSe quantum-dot-sensitized solar cell with ~100% internal quantum efficiency. *ACS Nano* 4:6377–6386. <https://doi.org/10.1021/nn101319x>
15. Gao W, Emaminejad S, Nyein HYY, Challa S, Chen K, Peck A, Fahad HM, Ota H, Shiraki H, Kiriya D et al (2016) Fully integrated wearable sensor arrays for multiplexed in situ perspiration analysis. *Nature* 529:509–514. <https://doi.org/10.1038/nature16521>

16. Göpel W, Schierbaum KD (1995) SnO₂ sensors: current status and future prospects. *Sens Actuators B* 26:1–12. [https://doi.org/10.1016/0925-4005\(94\)01546-T](https://doi.org/10.1016/0925-4005(94)01546-T)
17. Hao E, Sun H, Zhou Z, Liu J, Yang B, Shen J (1999) Synthesis and optical properties of CdSe and CdSe/CdS nanoparticles. *Chem Mater* 11:3096–3102. <https://doi.org/10.1021/cm990153p>
18. Hu Y, Zhang L, Li X, Liu R, Lin L, Zhao S (2017) Green preparation of S and N Co-doped carbon dots from water chestnut and onion as well as their use as an off–on fluorescent probe for the quantification and imaging of coenzyme A. *ACS Sustainable Chem Eng* 5:4992–5000. <https://doi.org/10.1021/acssuschemeng.7b00393>
19. Jonoobi M, Oladi R, Davoudpour Y, Oksman K, Dufresne A, Hamzeh Y, Davoodi R (2015) Different preparation methods and properties of nanostructured cellulose from various natural resources and residues: a review. *Cellulose* 22:935–969. <https://doi.org/10.1007/s10570-015-0551-0>
20. Kini S, Ganiga V, Kulkarni SD, Chidangil S, George SD (2018) Sensitive detection of mercury using the fluorescence resonance energy transfer between CdTe/CdS quantum dots and rhodamine 6G. *J Nanopart Res* 20:232. <https://doi.org/10.1007/s11051-018-4320-5>
21. Klimov VI, Mikhailovsky AA, Xu S, Malko A, Hollingsworth JA, Leatherdale CA, Eisler H, Bawendi MG (2000) Optical gain and stimulated emission in nanocrystal quantum dots. *Science* 290:314–317. <https://doi.org/10.1126/science.290.5490.314>
22. Li W, Ma S, Li Y, Yang G, Mao Y, Luo J, Gengzang D, Xu X, Yan S (2015) Enhanced ethanol sensing performance of hollow ZnO–SnO₂ core–shell nanofibers. *Sens Actuators B* 211:392–402. <https://doi.org/10.1016/j.snb.2015.01.090>
23. Liang Z, Kang M, Payne GF, Wang X, Sun R (2016) Probing energy and electron transfer mechanisms in fluorescence quenching of biomass carbon quantum dots. *ACS Appl Mater Interfaces* 8:17478–17488. <https://doi.org/10.1021/acsam.6b04826>
24. Liu H, Li M, Voznyy O, Hu L, Fu Q, Zhou D, Xia Z, Sargent EH, Tang J (2014b) Physically flexible, rapid-response gas sensor based on colloidal quantum dot solids. *Adv Mater* 26:2718–2724. <https://doi.org/10.1002/adma.201304366>
25. Liu L, Yu X, Yi Z, Chi F, Wang H, Yuan Y, Li D, Xu K, Zhang X (2019) High efficiency solar cells tailored using biomass-converted graded carbon quantum dots. *Nanoscale* 11:15083–15090. <https://doi.org/10.1039/c9nr05957a>
26. Meena R, Singh R, Marappan G, Kushwaha G, Gupta N, Meena R, Gupta JP, Agarwal RR, Fahmi N, Kushwaha OS (2019) Fluorescent carbon dots driven from ayurvedic medicinal plants for cancer cell imaging and phototherapy. *Heliyon* 5. <https://doi.org/10.1016/j.heliyon.2019.e02483>
27. Pan D, Zhang J, Li Z, Wu M (2010) Hydrothermal route for cutting graphene sheets into blue-luminescent graphene quantum dots. *Adv Mater* 22:734–738. <https://doi.org/10.1002/adma.200902825>
28. Qi H, Teng M, Liu M, Liu S, Li J, Yu H, Teng C, Huang Z, Liu H, Shao Q (2019) Biomass-derived nitrogen-doped carbon quantum dots: highly selective fluorescent probe for detecting Fe³⁺ ions and tetracyclines. *J Colloid Interface Sci* 539:332–341. <https://doi.org/10.1016/j.jcis.2018.12.047>

29. Ren HH, Fan Y, Wang B, Yu LP (2018) Polyethylenimine-capped CdS quantum dots for sensitive and selective detection of nitrite in vegetables and water. *J Agric Food Chem* 66:8851–8858. <https://doi.org/10.1021/acs.jafc.8b01951>
30. Robinson BH (2009) E-waste: An assessment of global production and environmental impacts. *Sci Total Environ* 408:183–191. <https://doi.org/10.1016/j.scitotenv.2009.09.044>
31. Schierbaum KD, Weimar U, Göpel W, Kowalkowski R (1991) Conductance, work function and catalytic activity of SnO₂-based gas sensors. *Sens Actuators B* 3:205–214. [https://doi.org/10.1016/0925-4005\(91\)80007-7](https://doi.org/10.1016/0925-4005(91)80007-7)
32. Silva AC, Freschi AP, Rodrigues CM, Matias BF, Maia LP, Goulart LR, Dantas NO (2016) Biological analysis and imaging applications of CdSe/CdS_xSe_{1-x}/CdS core-shell magic-sized quantum dot. *Nanomedicine: nanotechnology biology medicine* 12:1421–1430. <https://doi.org/10.1016/j.nano.2016.01.001>
33. Sun Q, Wu Z, Cao Y, Guo J, Long M, Duan H, Jia D (2019) Chemiresistive sensor arrays based on noncovalently functionalized multi-walled carbon nanotubes for ozone detection. *Sens Actuators B* 297:126689. <https://doi.org/10.1016/j.snb.2019.126689>
34. Wang GL, Jiao HJ, Zhu XY, Dong YM, Li ZJ (2012) Enhanced fluorescence sensing of melamine based on thioglycolic acid-capped CdS quantum dots. *Talanta* 93:398–403. <https://doi.org/10.1016/j.talanta.2012.02.062>
35. Wang L, Chen D, Jiang K, Shen G (2017) New insights and perspectives into biological materials for flexible electronics. *Chem Soc Rev* 46:6764–6815. <https://doi.org/10.1039/C7CS00278E>
36. Wang L, Li B, Xu F, Shi X, Feng D, Wei D, Li Y, Feng Y, Wang Y, Jia D, Sun W (2016a) High-yield synthesis of strong photoluminescent N-doped carbon nanodots derived from hydrosoluble chitosan for mercury ion sensing via smartphone APP. *Biosens Bioelectron* 79:1–8. <https://doi.org/10.1016/j.bios.2015.11.085>
37. Wang L, Li W, Wu B, Li Z, Wang S, Liu Y, Pan D, Wu M (2016b) Facile synthesis of fluorescent graphene quantum dots from coffee grounds for bioimaging and sensing. *Chem Eng J* 300:75–82. <https://doi.org/10.1016/j.cej.2016.04.123>
38. Wu Z, Zhou C, Zu B, Li Y, Dou X (2016) Contactless and rapid discrimination of improvised explosives realized by Mn²⁺ doping tailored ZnS nanocrystals. *Adv Funct Mater* 26:4578–4586. <https://doi.org/10.1002/adfm.201600592>
39. Zhang W, Wu Z, Hu J, Cao Y, Guo J, Long M, Duan H, Jia D (2020a) Flexible chemiresistive sensor of polyaniline coated filter paper prepared by spraying for fast and non-contact detection of nitroaromatic explosives. *Sens Actuators B* 304:127233. <https://doi.org/10.1016/j.snb.2019.127233>
40. Zhang W, Zhang X, Wu Z, Abdurahman K, Cao Y, Duan H, Jia D (2020b) Mechanical, electromagnetic shielding and gas sensing properties of flexible cotton fiber/polyaniline composites. *Compos Sci Technol* 188:107966. <https://doi.org/10.1016/j.compscitech.2019.107966>
41. Zhang Z, Xu M, Liu L, Ruan X, Yan J, Zhao W, Yun J, Wang Y, Qin S, Zhang T (2018) Novel SnO₂@ZnO hierarchical nanostructures for highly sensitive and selective NO₂ gas sensing. *Sens*

Figures

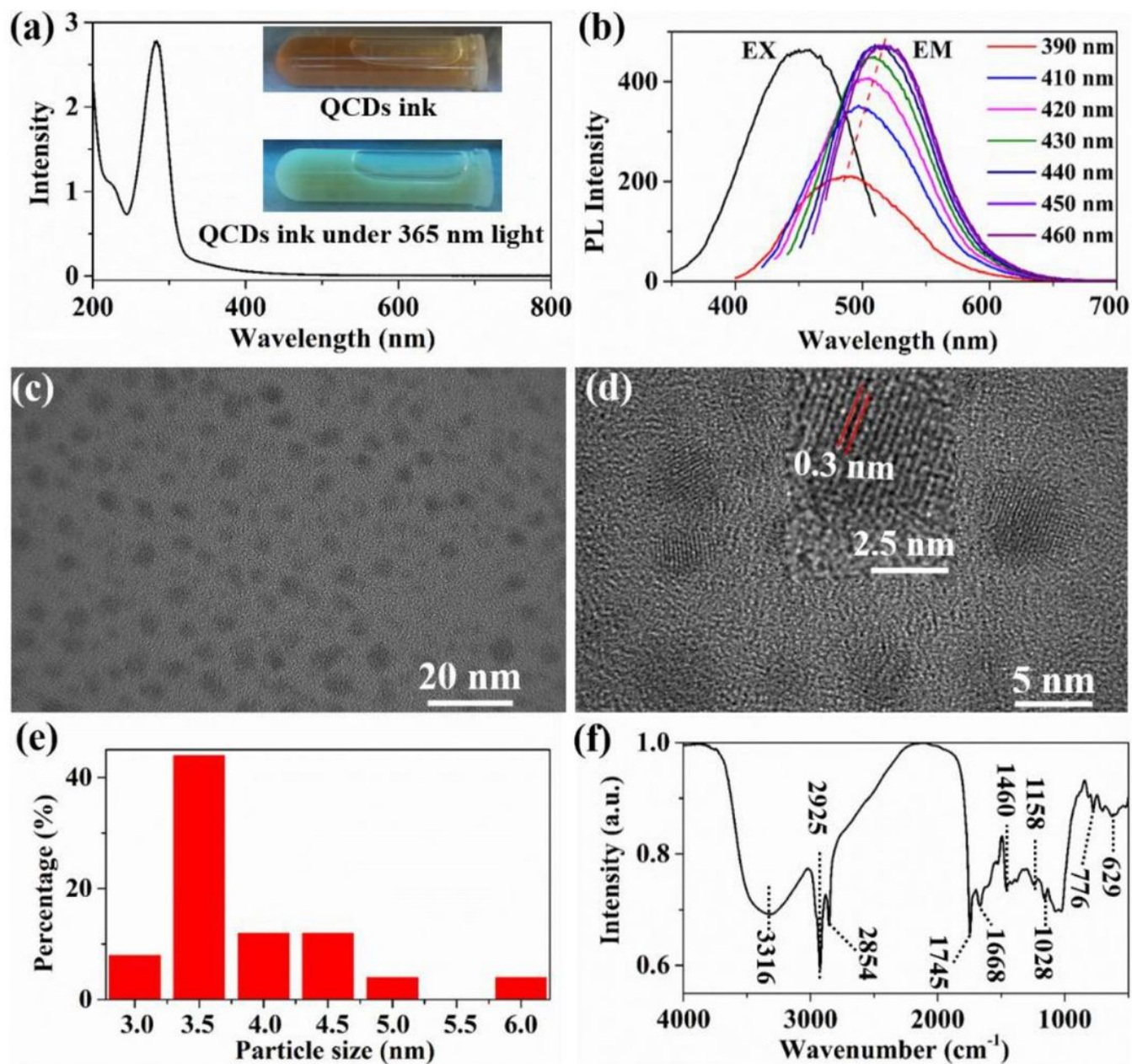


Figure 1

(a) UV-Vis absorption spectrum (inset: photograph of CQDs ink), (b) excitation spectra and excitation-independent emission spectra, (c, d) TEM and HRTEM image, (e) the size distribution and (f) FT-IR spectra of CQDs.

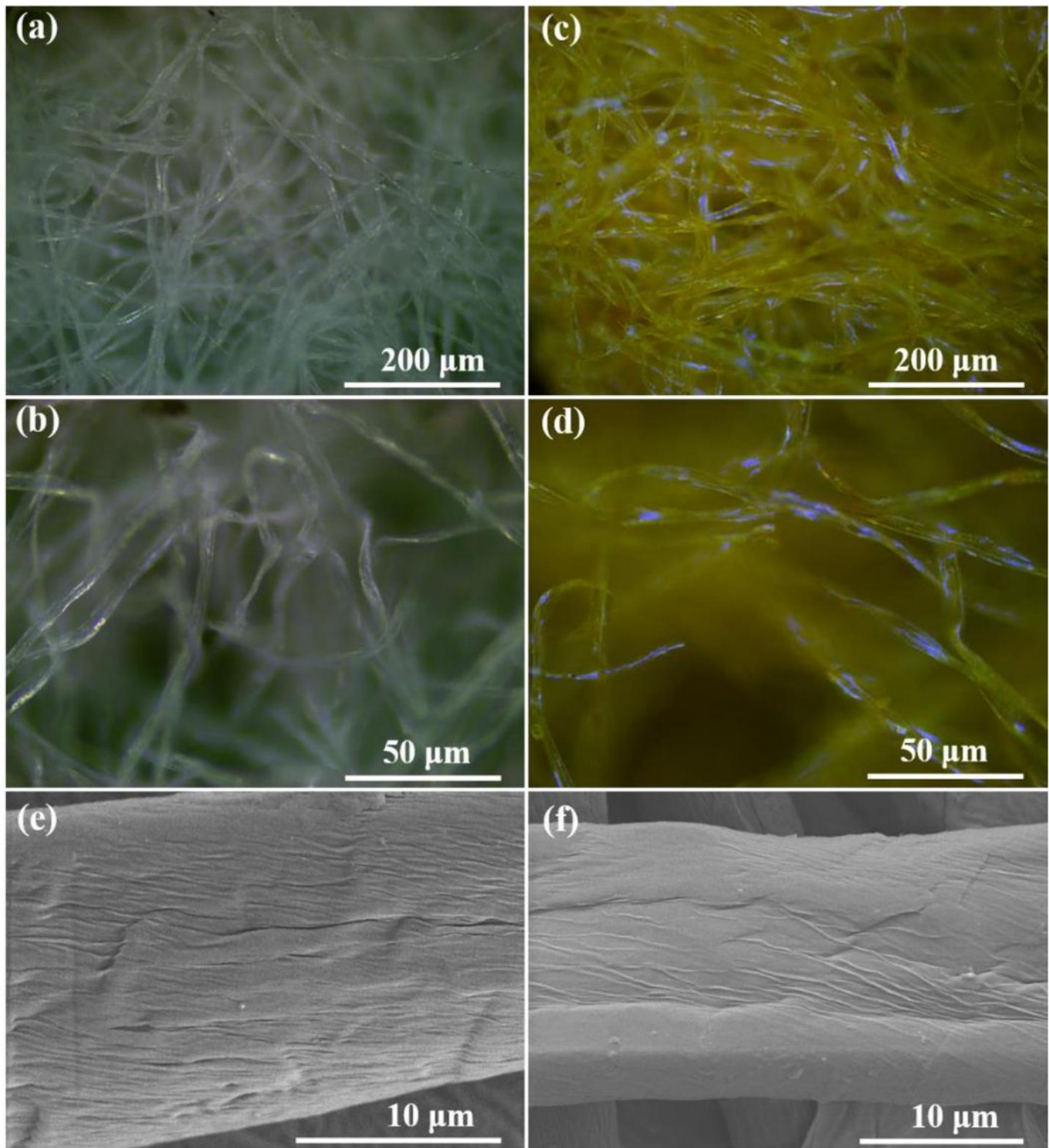


Figure 2

Light microscope images (a, b) PCFT film, (c, d) CQD/PCFT film; SEM images (e) PCFT fiber, (f) CQD/PCFT fiber.

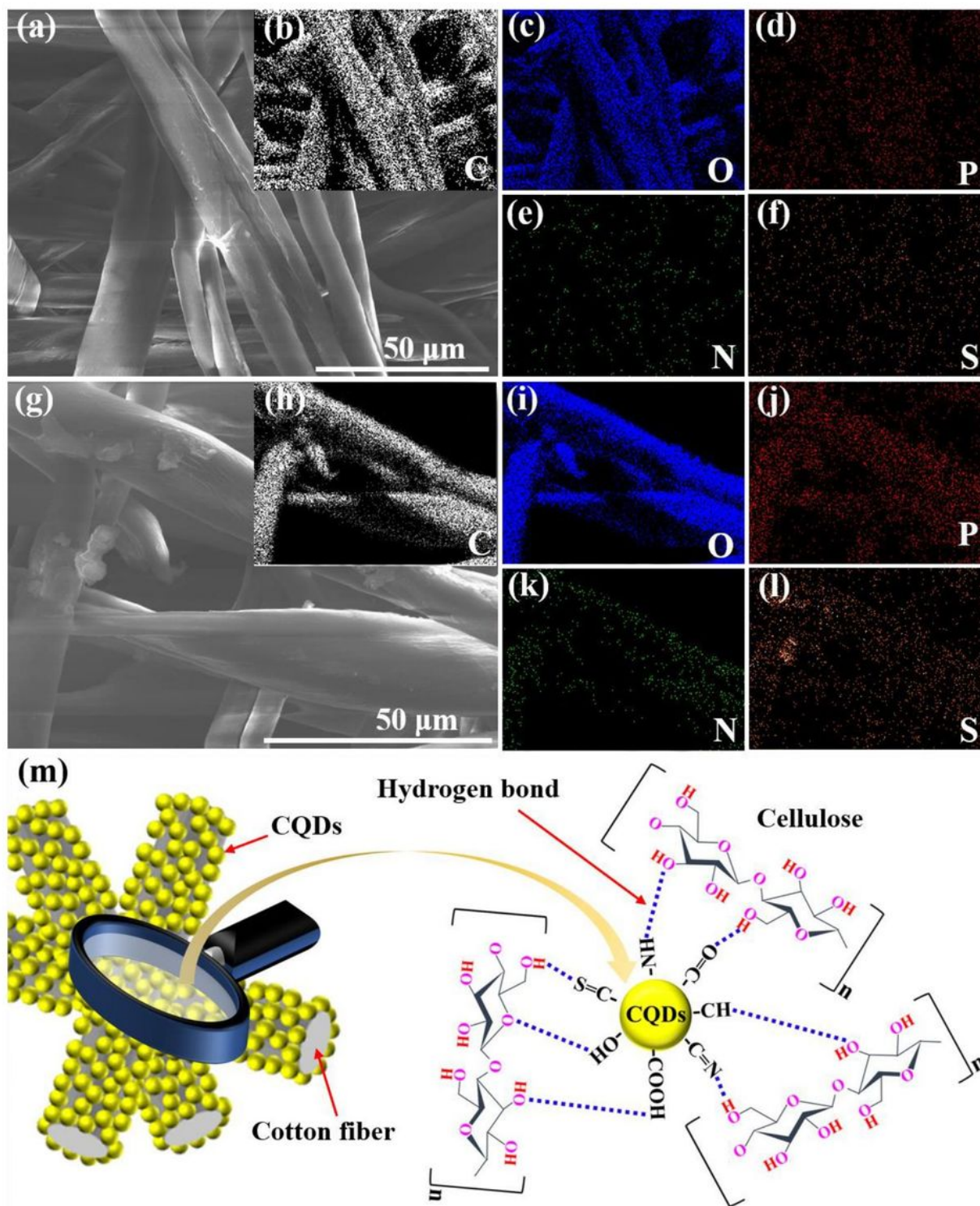


Figure 3

(a) SEM image of PCFT fibers, (b-f) Element mapping of PCFT, (g) SEM image of CQD/PCFT fibers, (h-l) Element mapping of CQD/PCFT, (m) Schematic diagram of CQDs adsorbed on cotton fiber through hydrogen bond interaction between CQDs and cellulose.

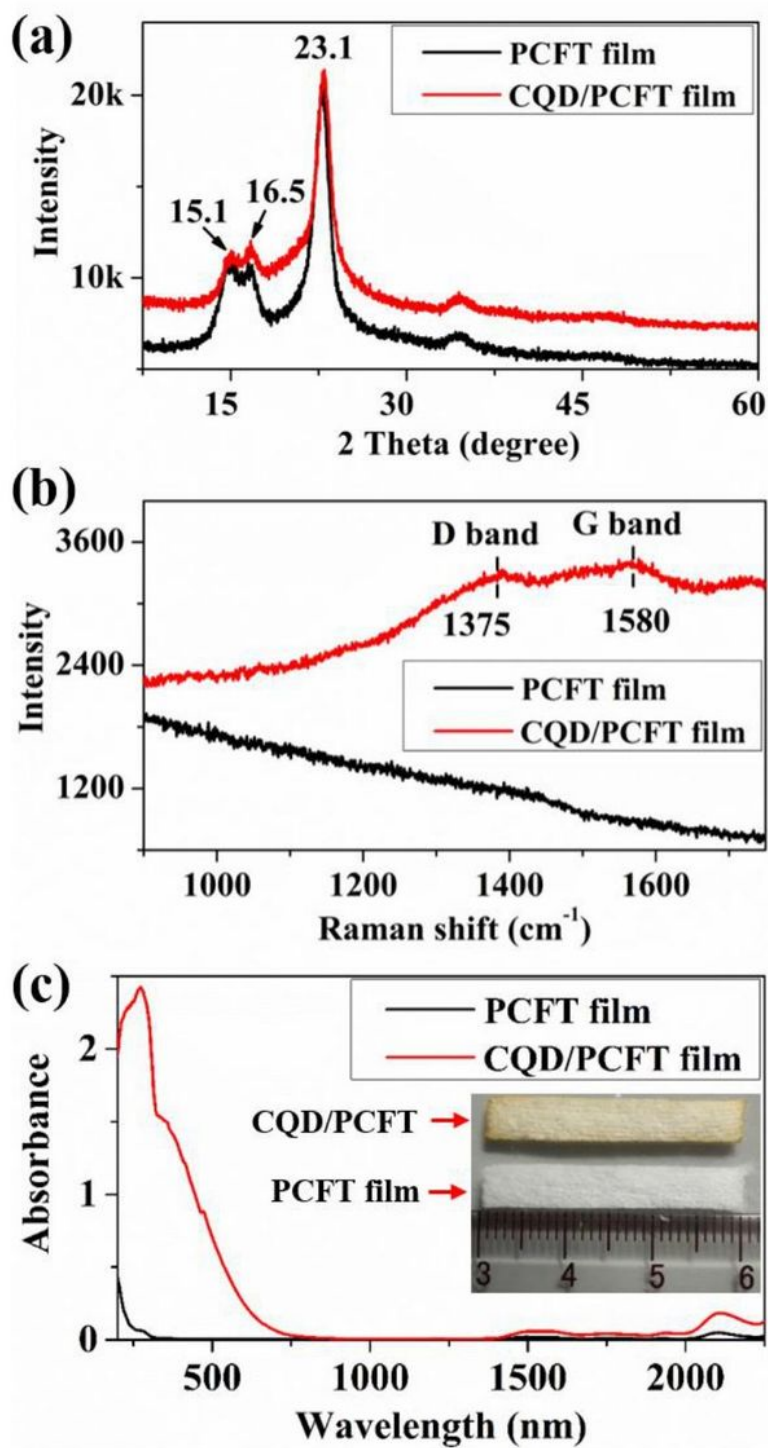


Figure 4

(a) XRD patterns, (b) Raman spectra and (c) UV-Vis spectra (inset: photograph of PCFT and CQD/PCFT).

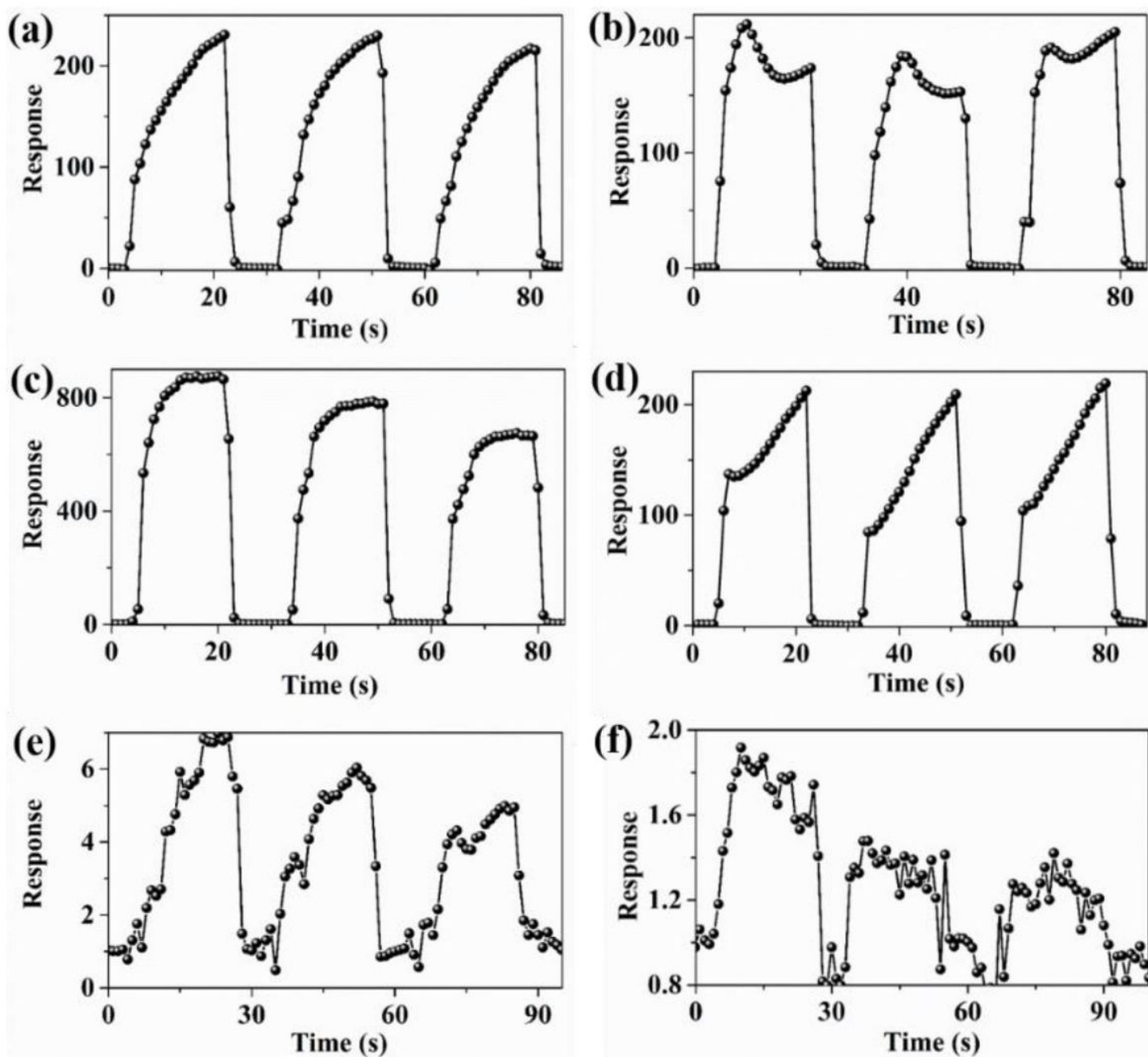


Figure 5

Sensing curves of flexible CQD/PCFT sensor without bending to (a) 85% RH, (b) 1000 ppm of NH_3 , (c) 1000 ppm of H_2O_2 , (d) 1000 ppm of CH_2O , (e) 1000 ppm of $\text{C}_2\text{H}_6\text{O}$, (f) 1000 ppm of $\text{C}_3\text{H}_6\text{O}$.

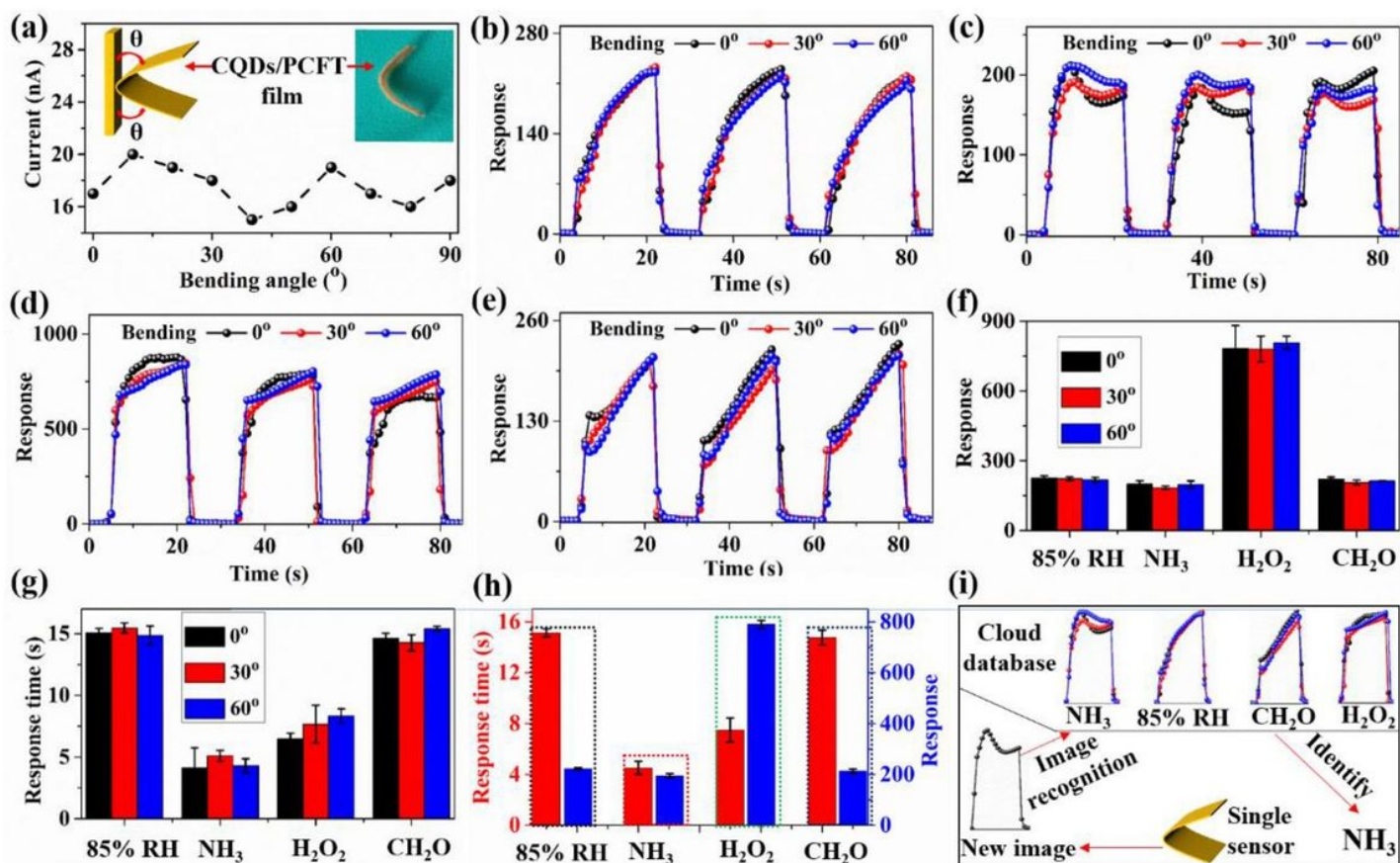


Figure 6

Bending stability of flexible CQD/PCFT sensor to (a) current changes of flexible CQD/PCFT sensor with the bending angle (insert: schematic diagram of bending test), (b) 85% RH, (c) 1000 ppm of NH₃, (d) 1000 ppm of H₂O₂, (e) 1000 ppm of CH₂O; (f) Response, (g) Response time, (h) Binary parameters (response time, response), (i) Schematic diagram of discriminative detection for single sensor.

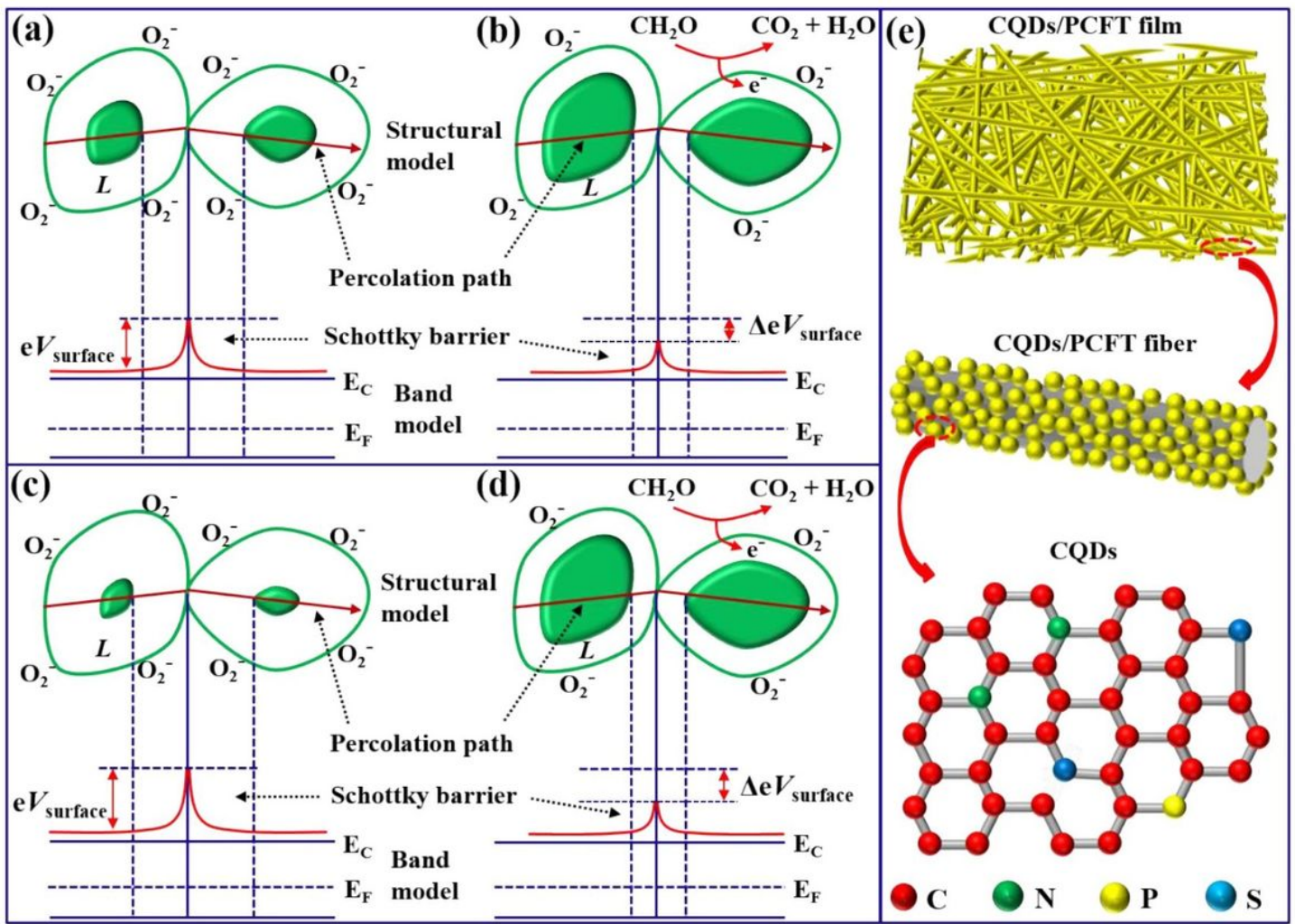


Figure 7

Structural and band model showing the role of contact regions between two adjacent sensing particles in determining the conductance over an N-type semiconductor: (a) initial state and (b) effect of CH_2O on L and eV_{surface} for large sensing particles, (c) initial state and (d) effect of CH_2O on L and eV_{surface} for small sensing particles, (e) schematic diagram of progressively enlarged CQDs/PCFT film.

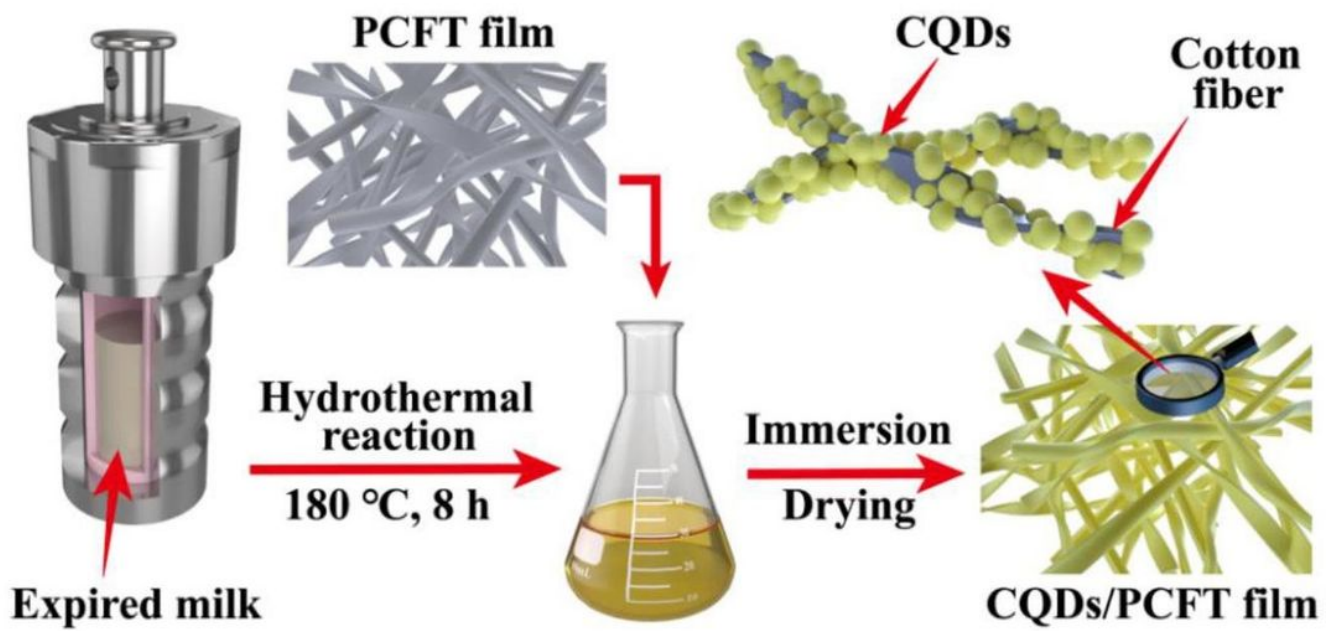


Figure 8

Schematic1. Schematic diagram of flexible CQD/PCFT film.